

Using CO line ratios to trace compressed areas in bubble N131

Chuan-Peng Zhang^{1,2,5}, Guang-Xing Li³, Chenlin Zhou^{1,4}, Lixia Yuan^{1,4}, and Ming Zhu^{1,5}

¹ National Astronomical Observatories, Chinese Academy of Sciences, 100101 Beijing, P.R. China
e-mail: cpzhang@nao.cas.cn

² Max-Planck-Institut für Astronomie, Königstuhl 17, D-69117 Heidelberg, Germany

³ South-Western Institute for Astronomy Research, Yunnan University, Kunming, 650500 Yunnan, P.R. China
e-mail: gxli@ynu.edu.cn

⁴ University of Chinese Academy of Sciences, 100049 Beijing, P.R. China

⁵ CAS Key Laboratory of FAST, National Astronomical Observatories, Chinese Academy of Sciences, 100101 Beijing, P.R. China

October 14, 2019

ABSTRACT

Aims. N131 is a typical infrared dust bubble showing an expanding ringlike shell. We study what kinds of CO line ratios can be used to trace the interaction in the expanding bubble.

Methods. We carry out new CO(3–2) observations towards bubble N131 using JCMT 15-m telescope, and derive line ratios by combining with our previous CO(2–1) and CO(1–0) data from IRAM 30-m observations. To trace the interaction between the molecular gas and the ionized gas in the HII region, we use RADEX to model the dependence of CO line ratios on kinetic temperature and H₂ volume density, and examine the abnormal line ratios based on other simulations.

Results. We present CO(3–2), CO(2–1), and CO(1–0) integrated intensity maps convolved to the same angular resolution (22.5"). The three different CO transition maps show apparently similar morphology. The line ratios of $W_{\text{CO}(3-2)}/W_{\text{CO}(2-1)}$ mostly range from 0.2 to 1.2 with a median of 0.54 ± 0.12 , while the line ratios of $W_{\text{CO}(2-1)}/W_{\text{CO}(1-0)}$ range from 0.5 to 1.6 with a median of 0.84 ± 0.15 . The high CO line ratios $W_{\text{CO}(3-2)}/W_{\text{CO}(2-1)} \gtrsim 0.8$ and $W_{\text{CO}(2-1)}/W_{\text{CO}(1-0)} \gtrsim 1.2$ are beyond the threshold predicted by numerical simulations based on the assumed density-temperature structure for the inner rims of ringlike shell, where are the compressed areas in bubble N131.

Conclusions. These high CO integrated intensity ratios, such as $W_{\text{CO}(3-2)}/W_{\text{CO}(2-1)} \gtrsim 0.8$ and $W_{\text{CO}(2-1)}/W_{\text{CO}(1-0)} \gtrsim 1.2$, can be used as a tracer of gas compressed regions with a relatively high temperature and density. This further suggests that the non-Gaussian part of the line-ratio distribution can be used to trace the interaction between the molecular gas and the hot gas in the bubble.

Key words. infrared: ISM – stars: formation – ISM: bubbles – H II regions – ISM clouds

1. Introduction

Infrared dust bubbles are ubiquitous interstellar objects (Churchwell et al. 2006, 2007; Simpson et al. 2012; Hou & Gao 2014; Zhang et al. 2013, 2016; Jayasinghe et al. 2019). However, the details of the bubble shell formation mechanism are not yet clear (e.g. Beaumont & Williams 2010; Watson et al. 2008). N131 is a quite typical bubble, which has been observed and investigated in detail by Zhang et al. (2013, 2016). The bubble N131 has an inner minor radius of 13 pc and inner major radius of 15 pc at a kinetic distance of ~ 8.6 kpc with a center coordinate of R.A.(J2000) = $19^{\text{h}}52^{\text{m}}21^{\text{s}}.5$, DEC.(J2000) = $+26^{\circ}21'24''.0$. A ringlike shell can be seen at 8.0 and $24\mu\text{m}$ associated with CO emission (see Figure 1). Two giant elongated molecular clouds are located at the opposite sides of the ringlike shell, and altogether, they exhibit a large velocity gradient. In addition, there is a huge cavity inside the bubble seen in the $5.8 - 500\mu\text{m}$ emission. The column density, excitation temperature, and velocity of CO(1–0) emission show a possibly stratified structure from the inner to outer rims of the ring-like shell. These suggest that the bubble N131 has an expanding shell caused by a feedback of strong stellar winds from the star formation at the bubble center (see also detailed discussion in Zhang et al. 2016).

The CO(3–2), CO(2–1), and CO(1–0) transitions have different upper energy levels (Kaufman et al. 1999). Thus, the different transitions can be used to trace different

excitation conditions. The integrated intensity ratios, such as $W_{\text{CO}(3-2)}/W_{\text{CO}(2-1)}$ and $W_{\text{CO}(2-1)}/W_{\text{CO}(1-0)}$, may indicate different temperature and density structure of molecular cloud environments (Hasegawa et al. 1994; Wilson et al. 1997). For example, high $W_{\text{CO}(2-1)}/W_{\text{CO}(1-0)}$ ratios were already observed in the Large Magellanic Cloud (LMC) by Bolatto et al. (2000). It was proposed that self-absorbed emission and optical depth effects may be possible origins for the high line ratios (Bolatto et al. 2000, 2003). Additionally, the line ratios are also quite important for us to diagnose the evolutionary stage of the molecular clouds (e.g., Sakamoto et al. 1995; Beuther et al. 2000; Yoda et al. 2010; Polychroni et al. 2012; Nishimura et al. 2015).

In this work, we carry out new CO(3–2) observations towards bubble N131 using JCMT 15-m telescope. In combination with our previous CO(2–1) and CO(1–0) line observations from IRAM 30-m telescope, we study how the CO line ratios can be used to trace the interaction in the expanding infrared dust bubble N131. In Section 2, we describe the observations and data reduction. In Section 3, we show the observational results, and RADEX modelling. In Section 4, we mainly discuss the possibility of using the CO line ratios to trace the compressed inner rims of the ringlike shell around the bubble. In Section 5, we give a summary.

2. Observations

2.1. $^{12}\text{CO } J = 3 - 2$

We carried out new CO (3 – 2) observations (Nos. M17BP077 and M18BP069) towards the bubble N131 during September 2017 – August 2018 using the Heterodyne Array Receiver Programme (HARP; Buckle et al. 2009) in the JCMT 15-m telescope. Maps were referenced against an off-source position, which is free of any significant CO emission in the Dame et al. (2001) CO Galactic Plane Survey. At 345 GHz, the half-power beam width (HPBW) was $\sim 14.0''$, and the main beam efficiency is $\eta_{\text{mb}} = 0.64$, taken from the JCMT efficiency archive. The main beam brightness temperature (T_{mb}) can be derived by $T_{\text{mb}} = T_{\text{A}}^* / \eta_{\text{mb}}$. The on-the-fly mapping mode was used to scan the bubble with a sampling step of $7.0''$. For further line ratio analysis, the raw data were then convolved to the same angular resolution of $22.5''$, corresponding to the lowest angular resolution of CO (1 – 0) (see Section 2.2), with a grid of $11.0''$ using the GILDAS¹ software package.

Calibration scans, pointing, and focus were performed regularly. Calibration scans were taken at the beginning of each subscan. A pointing was done about every hour. A focus scan was taken every three hours but with more scans taken around sunset and sunrise. The flux calibration is expected to be accurate within 10%. The GILDAS software package was used to reduce the observational data.

2.2. $^{12}\text{CO } J = 2 - 1$ and $J = 1 - 0$

Our CO (2 – 1) and CO (1 – 0) observations were simultaneously carried out during April 2014 using the IRAM 30-m telescope² on Pico Veleta, Spain. The observations have been introduced in detail in our previous work of Zhang et al. (2016). In our raw data, the HPBWs of CO (2 – 1) and CO (1 – 0) are, respectively, $11.3''$ and $22.5''$ with the same sampling step of $9.3''$. For further line ratio analysis, the raw data were then convolved to the lowest angular resolution of $22.5''$ with a grid of $11.0''$ using the GILDAS software package.

3. Results and analysis

3.1. CO integrated intensity distributions

Figure 1 displays the integrated intensity maps of CO (3 – 2), CO (2 – 1), and CO (1 – 0) lines with a velocity range from -16.0 to -5.0 km s^{-1} superimposed on MIPS GAL $24 \mu\text{m}$ emission (Carey et al. 2009). All the CO data have been convolved to the same angular resolution of $22.5''$. We also label the nine selected molecular clumps (Zhang et al. 2016) and the ringlike shell of the bubble in the maps. The morphological structures of the three integrated intensity maps are obviously similar.

3.2. Spectra

We extract several example spectra CO (3 – 2), CO (2 – 1), and CO (1 – 0) (see upper panels in Figures 2 and 3) with high ratios ($W_{\text{CO}(3-2)}/W_{\text{CO}(2-1)} \gtrsim 0.8$ and $W_{\text{CO}(2-1)}/W_{\text{CO}(1-0)} \gtrsim 1.2$) from bubble inner rims near clumps A, B, G and H. All the spectra with the highest ratios have high signal-to-noise ratios above

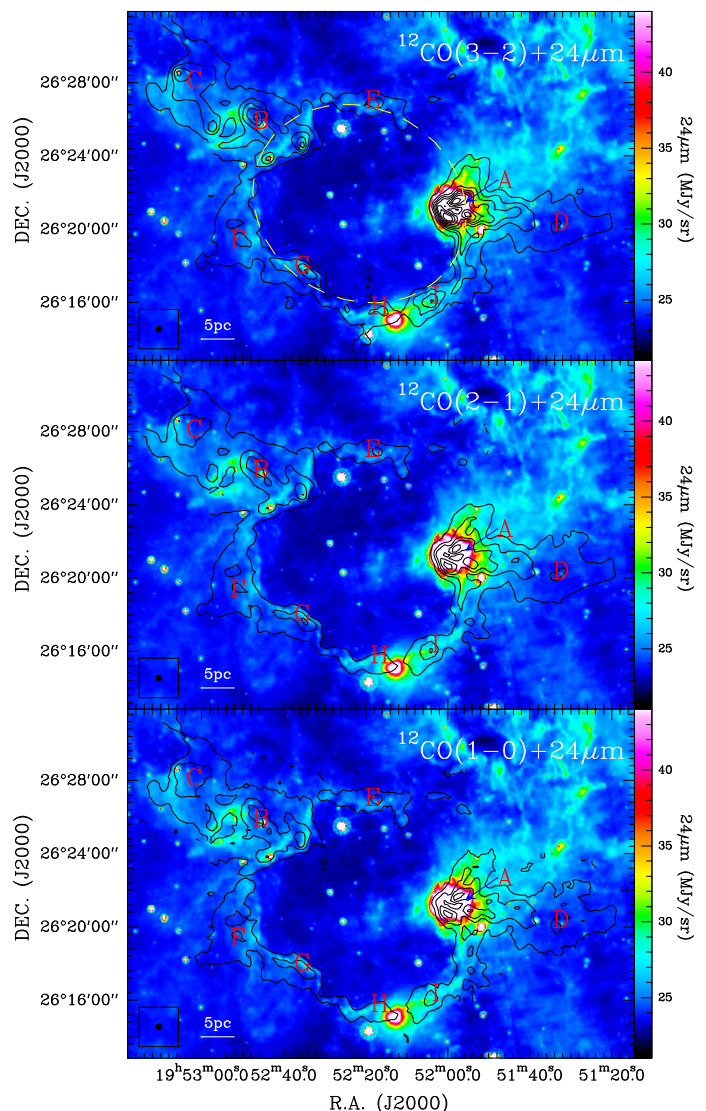


Fig. 1. Integrated intensity maps of CO (3 – 2) (upper), CO (2 – 1) (middle), and CO (1 – 0) (lower) lines with a velocity range from -16.0 to -5.0 km s^{-1} superimposed on $24 \mu\text{m}$ emission. The contour levels in each CO map start at 5σ in steps of 10σ with $\sigma_{\text{CO}(3-2)} = 0.6 \text{ K km s}^{-1}$, $\sigma_{\text{CO}(2-1)} = 1.3 \text{ K km s}^{-1}$, and $\sigma_{\text{CO}(1-0)} = 1.6 \text{ K km s}^{-1}$. The letters, and ellipse indicate the positions of nine molecular clumps (A, B, ..., and I), and ringlike shell of the bubble, respectively. The angular resolution ($22.5''$) is indicated at the bottom-left corner of each subfigure.

10σ . This indicates that the line ratios have high signal-to-noise ratios at least above 7σ . For comparison, we also extract some spectra (see lower panels in Figure 2 and 3) with low line ratios from the corresponding clump center regions.

3.3. Integrated intensity ratio distributions

Figure 4 displays the integrated intensity ratio maps of $W_{\text{CO}(3-2)}/W_{\text{CO}(2-1)}$ and $W_{\text{CO}(2-1)}/W_{\text{CO}(1-0)}$. The ratios were obtained based on the integrated intensity maps that are above 5σ (see Figure 1). For the line ratios we consider pixels above 3.5σ according to the propagation of errors of the integrated intensity maps. It clearly shows that at the clumps A, F, G, H, and I in the $W_{\text{CO}(3-2)}/W_{\text{CO}(2-1)}$ map, the inner rims of ringlike shell have a higher integrated intensity ratio ($W_{\text{CO}(3-2)}/W_{\text{CO}(2-1)} \gtrsim 0.8$) than the outer rims, while in the $W_{\text{CO}(2-1)}/W_{\text{CO}(1-0)}$ map the highest

¹ <http://www.iram.fr/IRAMFR/GILDAS/>

² Based on observations carried out with the IRAM 30-m Telescope. IRAM is supported by INSU/CNRS (France), MPG (Germany) and IGN (Spain).

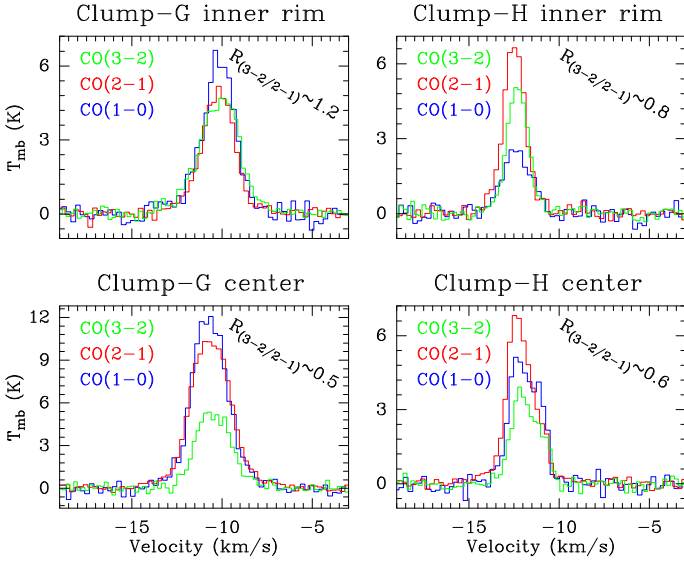


Fig. 2. Example spectra of high ratios $W_{\text{CO}(3-2)}/W_{\text{CO}(2-1)}$ (upper) from bubble inner rims of the ringlike shell near clumps G and H, and low ratios (lower) from the clump center regions (see also Figure 4).

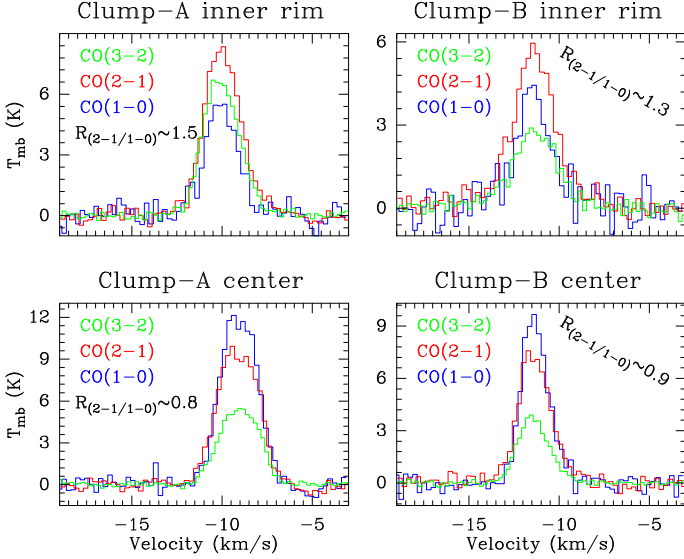


Fig. 3. Example spectra of high ratios $W_{\text{CO}(2-1)}/W_{\text{CO}(1-0)}$ (upper) from bubble inner rims of the ringlike shell near clumps A and B, and low ratios (lower) from the clump center regions (see also Figure 4).

line ratio happens at the inner rims of the shell near clumps A, B, E, and F with $W_{\text{CO}(2-1)}/W_{\text{CO}(1-0)} \gtrsim 1.2$. Figures 2 and 3 display some spectra CO(3–2), CO(2–1), and CO(1–0) extracted from bubble inner rims of the ringlike shell near clumps A, B, G and H where have high ratios ($W_{\text{CO}(3-2)}/W_{\text{CO}(2-1)} \gtrsim 0.8$ and $W_{\text{CO}(2-1)}/W_{\text{CO}(1-0)} \gtrsim 1.2$).

Figure 5 displays the integrated intensity ratio histograms of $W_{\text{CO}(3-2)}/W_{\text{CO}(2-1)}$ and $W_{\text{CO}(2-1)}/W_{\text{CO}(1-0)}$ for all pixels in Figure 4. The line ratios of $W_{\text{CO}(3-2)}/W_{\text{CO}(2-1)}$ mostly range from 0.2 to 1.2 with a median of 0.54 ± 0.12 , which is slightly lower than what was found (≈ 0.75) at the Central Molecular Zone of the Milky Way (Kudo et al. 2011). The line ratios of $W_{\text{CO}(2-1)}/W_{\text{CO}(1-0)}$ range from 0.5 to 1.6 with a median of 0.84 ± 0.15 . We have also derived the median value of $W_{\text{CO}(3-2)}/W_{\text{CO}(1-0)}$ is around 0.45, close to the average value of

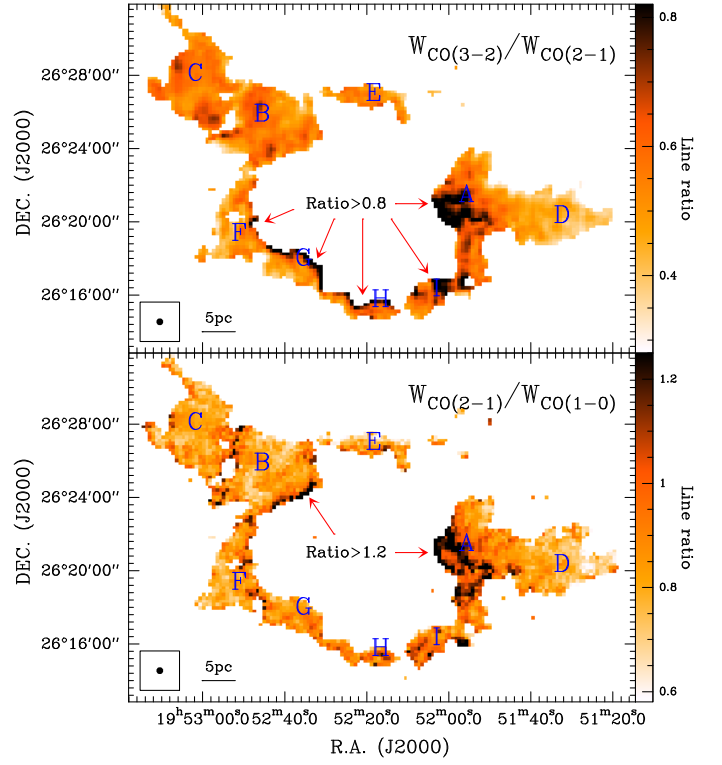


Fig. 4. Integrated intensity ratio maps of $W_{\text{CO}(3-2)}/W_{\text{CO}(2-1)}$ (upper) and $W_{\text{CO}(2-1)}/W_{\text{CO}(1-0)}$ (lower) derived from the integrated intensity maps that are above 5σ in Figure 1. The letters indicate the positions of nine molecular clumps (A, B, ..., and I) in the bubble. The angular resolution is indicated at the bottom-left corner of each subfigure.

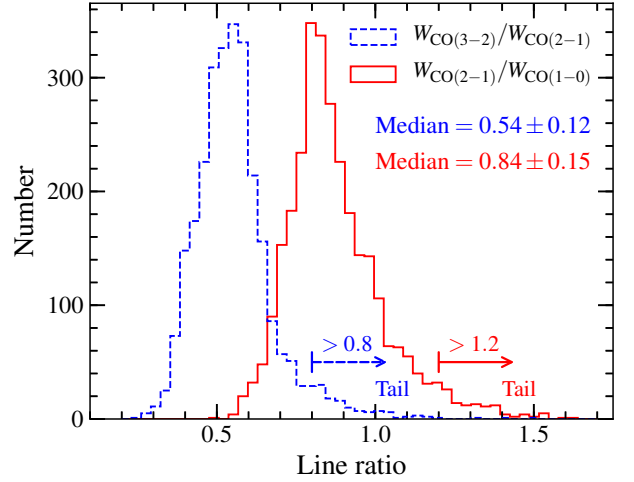


Fig. 5. Integrated intensity ratio histograms of $W_{\text{CO}(3-2)}/W_{\text{CO}(2-1)}$ and $W_{\text{CO}(2-1)}/W_{\text{CO}(1-0)}$ for all pixels in Figure 4. The median uncertainties are derived from the standard deviation of sample.

$W_{\text{CO}(3-2)}/W_{\text{CO}(1-0)} \approx 0.5$ in star forming galaxies (e.g. Aravena et al. 2010, 2014; Daddi et al. 2015).

3.4. RADEX modelling

To study the line ratio distributions as a function of kinetic temperature and H_2 volume density in bubble N131, we use the non-local thermodynamic equilibrium (non-LTE) radiative transfer

code RADEX³ (van der Tak et al. 2007) with the Leiden Atomic and Molecular Database (LAMDA; Schöier et al. 2005) to model CO (3 – 2), CO (2 – 1), and CO (1 – 0) lines. The model grid extends over a grid of 51 temperatures ($T_{\text{kin}} = 3 - 500$ K) and 51 densities ($n_{\text{H}_2} = 10 - 10^5 \text{ cm}^{-3}$). The CO column density and line width are fixed with $N_{\text{CO}} = 2.2 \times 10^{17} \text{ cm}^{-2}$ and $\delta v = 3.5 \text{ km s}^{-1}$, which are the derived median values of CO column density and CO (1 – 0) velocity dispersion from CO (1 – 0) and ^{13}CO (1 – 0) in N131 (see Zhang et al. 2016). The beam-filling factors are assumed to be unity.

Figures 6 and 7 display the line ratio and optical depth distributions as a function of kinetic temperature and H_2 volume density obtained with RADEX modelling. Linear molecules CO at low rotational transitions (critical density of about $n_{\text{crit}} \sim 10^4 \text{ cm}^{-3}$) are tracers of low density gas (Kaufman et al. 1999; Qin et al. 2008; Nishimura et al. 2015; Peñaloza et al. 2018). For a given molecule, moving up to a high rotational transition will lead to a high critical density. The high rotational transitions are sensitive to a high temperature based on the large velocity gradient (LVG) model. One thus can probe the high temperature and density with the high CO line ratios (van der Tak et al. 2007).

4. Discussion: Line ratios tracing the compressed areas

Wilson et al. (1997) found that the $W_{\text{CO}(3-2)}/W_{\text{CO}(2-1)}$ line ratios for the molecular clouds containing optical H II regions (0.79 ± 0.05) are somewhat higher than those for the clouds without optical H II regions (0.58 ± 0.06), while the line ratio in the giant H II region is even higher (1.07 ± 0.03). Wilson et al. (1997) also suggested that the high line ratio may be caused by heating of the gas by the massive stars. Line ratio distributions, such as $W_{\text{CO}(3-2)}/W_{\text{CO}(2-1)}$ and $W_{\text{CO}(2-1)}/W_{\text{CO}(1-0)}$, have been used to study the interaction in supernova remnant molecular cloud system (e.g. Jiang et al. 2010; Zhou et al. 2016, 2018; Arias et al. 2019). The high ratios with $W_{\text{CO}(2-1)}/W_{\text{CO}(1-0)} \approx 1.6$ were suggested by Zhou et al. (2016) as tracing the shocked compressed gas located at the shell of supernova remnant Tycho. Recently, Celis Peña et al. (2019) also found that the high integrated line ratios $W_{\text{CO}(3-2)}/W_{\text{CO}(2-1)}$ at the shell of the LMC supergiant bubble N11 may be resulted from the expansion of nebulae and the interaction with radiation from OB association. Why and how can the CO line ratios be used to trace the interactions?

The infrared dust bubble N131 originates from an expanding H II regions, yet the H II region insides has been extinguished (Zhang et al. 2013, 2016). In Figure 4, it clearly shows that the most parts of the inner rims of ringlike shell have higher integrated intensity ratios (e.g., $W_{\text{CO}(3-2)}/W_{\text{CO}(2-1)} \gtrsim 0.8$, $W_{\text{CO}(2-1)}/W_{\text{CO}(1-0)} \gtrsim 1.2$) than the outer rims. Additionally, the most notable discrepancy between the two ratio distributions is that at the inner rims of the ringlike shell near clumps G and H, the ratio $W_{\text{CO}(3-2)}/W_{\text{CO}(2-1)}$ is much higher than other regions (except the complicated clump A⁴) but the ratio $W_{\text{CO}(2-1)}/W_{\text{CO}(1-0)}$ is not, while at the inner rims near clump B, the ratio $W_{\text{CO}(2-1)}/W_{\text{CO}(1-0)}$ is much higher than other regions but the ratio $W_{\text{CO}(3-2)}/W_{\text{CO}(2-1)}$ is not. This may suggest that the inner rims of the ringlike shell near clumps G and H have a relatively high kinetic temperature up to the excitation temperature of high transition level of CO (3 – 2), leading to stronger CO (3 – 2) emission than other regions; while the inner rims near

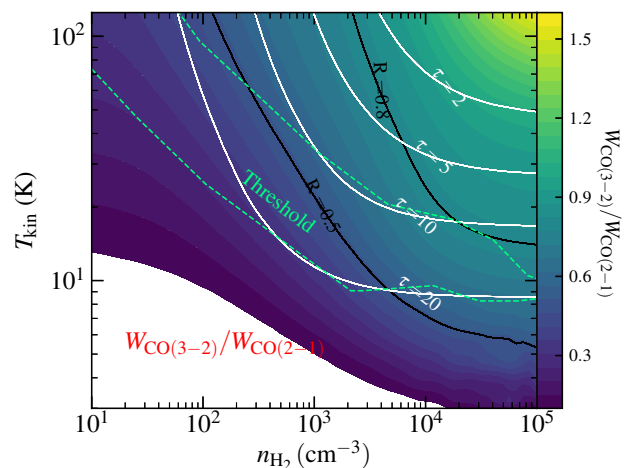


Fig. 6. Line ratios ($R = W_{\text{CO}(3-2)}/W_{\text{CO}(2-1)}$) and optical depths ($\tau_{\text{CO}(2-1)}$) in the conditions of $N_{\text{CO}} = 2.2 \times 10^{17} \text{ cm}^{-2}$ and $\delta v = 3.5 \text{ km s}^{-1}$ (estimated by median values in N131) as a function of kinetic temperature and volume density by RADEX modelling. The green contour indicates a region (or threshold) for a possible gas temperature-density distribution in a colliding flow at the onset of star formation from simulations in Clark et al. (2012).

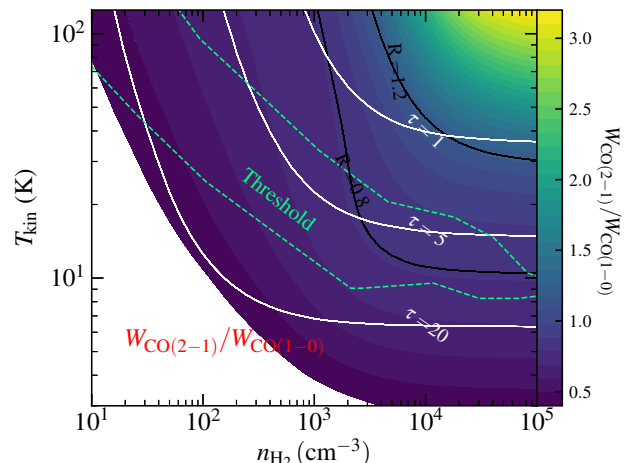


Fig. 7. Line ratios ($R = W_{\text{CO}(2-1)}/W_{\text{CO}(1-0)}$) and optical depths ($\tau_{\text{CO}(1-0)}$) in the conditions of $N_{\text{CO}} = 2.2 \times 10^{17} \text{ cm}^{-2}$ and $\delta v = 3.5 \text{ km s}^{-1}$ (estimated by median values in N131) as a function of kinetic temperature and volume density by RADEX modelling. The green contour indicates a region (or threshold) for a possible gas temperature-density distribution in a colliding flow at the onset of star formation from simulations in Clark et al. (2012).

clump B have a relatively low kinetic temperature just up to the low transition level of CO (2 – 1), leading to stronger CO (2 – 1) emission than other regions. This fact above also suggests that the inner rims of the ringlike shell were compressed by strong stellar winds from the bubble insides (see also discussion in Nishimura et al. 2015).

To trace the compressed inner rims of the ringlike shell by stellar winds from the bubble insides, using RADEX code, we computed the expected CO line ratios at different gas temperatures and densities. The results are presented in Figures 6 and 7. What kinds of CO line ratios can be used to trace the interactions? We remind the reader that in an “ordinary” molecular cloud, the cold gas is mainly heated by cosmic ray heating

³ <https://home.strw.leidenuniv.nl/~moldata/radex.html>

⁴ Clump A is actually a small expanding H II region deeply embedded in the ringlike shell of bubble N131 (see details in Zhang et al. 2016).

which is balanced by radiative cooling (Draine 2011). As a result, we expect a limited range of temperatures and densities for the molecular gas, which leads to a limited range of observed line ratios. These line ratios far beyond the upper limit could trace the interaction between the cold gas and the hot gas which reside presumably in the inner rims of a bubble shell since these interactions should lead to increase in temperature and density.

Therefore, we propose to use CO line ratios, $W_{\text{CO}(3-2)}/W_{\text{CO}(2-1)} \gtrsim 0.8$ and $W_{\text{CO}(2-1)}/W_{\text{CO}(1-0)} \gtrsim 1.2$, to trace the compressed inner rims of the ring-like shell. The thresholds are selected based on following considerations. The thresholds correspond to the non-Gaussian tail of line ratio distribution presented in Figure 5, where we propose that a non-interacting clouds should produce line ratios that are in Gaussian distribution, and the non-Gaussian parts of the distributions are caused by interaction. To justify our thresholds, using RADEX, we compute the line ratios as a function of gas temperature and density (see Figures 6 and 7). By overlaying the expected range of gas density and temperature found in the state-of-the-art numerical simulations⁵ (Clark et al. 2012), we derive the expected CO line ratios for non-interacting clouds. The highest ratios are located in regions with moderate/low optical depths ($\tau \lesssim 5$ for $W_{\text{CO}(3-2)}/W_{\text{CO}(2-1)} \gtrsim 0.8$ and $\tau \lesssim 1$ for $W_{\text{CO}(2-1)}/W_{\text{CO}(1-0)} \gtrsim 1.2$) in the temperature-density plane. Line ratios higher than this can be used to trace the interaction region where the gas temperature and density can be higher than normal.

5. Summary

Based on our previous multiwavelength observations (Zhang et al. 2013, 2016), infrared dust bubble N131 is a typical bubble showing an expanding ringlike shell, which has been swept up by the energetic winds of ionizing stars insides. In this work, we carried out new CO (3 – 2) observations towards the bubble N131 using JCMT 15-m telescope, and also used our published CO (2 – 1) and CO (1 – 0) line data observed by IRAM 30-m telescope. We plotted their integrated intensity maps, which were convolved to the same angular resolution (22.5"). We find that the three different CO transition maps show a similar morphological structure.

In the bubble N131, we use RADEX code to model kinetic temperature and H_2 volume density, and studied the relationship between them and line ratios. The line ratios of $W_{\text{CO}(3-2)}/W_{\text{CO}(2-1)}$ mostly range from 0.2 to 1.2 with a median of 0.54 ± 0.12 , while the line ratios of $W_{\text{CO}(2-1)}/W_{\text{CO}(1-0)}$ range from 0.5 to 1.6 with a median of 0.84 ± 0.15 . The linewidth ratios between CO (3 – 2), CO (2 – 1), and CO (1 – 0) are close to unity.

To probe the interaction between the hot stellar winds and the cold molecular ringlike shell, we perform RADEX modelling to test the dependence of line ratios on the underlying parameters such as temperature and density, and to predict the range of CO integrated intensity ratios $W_{\text{CO}(3-2)}/W_{\text{CO}(2-1)}$ and $W_{\text{CO}(2-1)}/W_{\text{CO}(1-0)}$ if the gas has the temperatures and densities predicted by the chemo-dynamics simulations. Line ratios far beyond the temperature-density threshold (Clark et al. 2012) could thus be used to trace the interactions.

⁵ Although the simulations in Clark et al. (2012) are carried out under a certain set of initial conditions, the predicted temperature-density relation for the molecular gas is relatively robust (e.g. independent on the initial condition) and is applicable to us. Additionally, due to the short cooling times, the density-temperature relation of the molecular gas should not depend on the initial conditions (e.g. whether the converging speed is fast or slow).

From our observations, we find that the high CO integrated intensity ratios $W_{\text{CO}(3-2)}/W_{\text{CO}(2-1)}$ and $W_{\text{CO}(2-1)}/W_{\text{CO}(1-0)}$ are far beyond the prediction from state-of-the-art numerical simulation without stellar feedback. As a result, these high line ratios can be used to trace the compressed areas in bubble N131. We suggest that the high CO integrated intensity ratios, such as $W_{\text{CO}(3-2)}/W_{\text{CO}(2-1)} \gtrsim 0.8$ and $W_{\text{CO}(2-1)}/W_{\text{CO}(1-0)} \gtrsim 1.2$, can be used as a tracer of gas compressed regions with a relatively high temperature and density. We further prove that the non-Gaussian part of the line-ratio distribution can be used to trace the interaction between the molecular gas and the hot gas in the bubble.

Acknowledgements. We thank the anonymous referees for constructive comments that improved the manuscript. This work is supported by the National Natural Science Foundation of China Nos. 11703040, 11743007, and National Key Basic Research Program of China (973 Program) No. 2015CB857101. C.-P. Zhang acknowledges support by the MPG-CAS Joint Doctoral Promotion Program (DPP) and China Scholarship Council (CSC) in Germany as a post-doctoral researcher. The JCMT is operated by the EAO on behalf of NAOJ; ASIAA; KASI; CAMS as well as the National Key R&D Program of China (No. 2017YFA0402700). Additional funding support is provided by the STFC and participating universities in the UK and Canada.

References

- Aravena, M., Carilli, C., Daddi, E., et al. 2010, *ApJ*, 718, 177
- Aravena, M., Hodge, J. A., Wagg, J., et al. 2014, *MNRAS*, 442, 558
- Arias, M., Domček, V., Zhou, P., & Vink, J. 2019, *A&A*, 627, A75
- Beaumont, C. N. & Williams, J. P. 2010, *ApJ*, 709, 791
- Beuther, H., Kramer, C., Deiss, B., & Stutzki, J. 2000, *A&A*, 362, 1109
- Bolatto, A. D., Jackson, J. M., Israel, F. P., Zhang, X., & Kim, S. 2000, *ApJ*, 545, 234
- Bolatto, A. D., Leroy, A., Israel, F. P., & Jackson, J. M. 2003, *ApJ*, 595, 167
- Buckle, J. V., Hills, R. E., Smith, H., et al. 2009, *MNRAS*, 399, 1026
- Carey, S. J., Noriega-Crespo, A., Mizuno, D. R., et al. 2009, *PASP*, 121, 76
- Celis Peña, M., Paron, S., Rubio, M., Herrera, C. N., & Ortega, M. E. 2019, *arXiv e-prints*, arXiv:1905.08829
- Churchwell, E., Povich, M. S., Allen, D., et al. 2006, *ApJ*, 649, 759
- Churchwell, E., Watson, D. F., Povich, M. S., et al. 2007, *ApJ*, 670, 428
- Clark, P. C., Glover, S. C. O., Klessen, R. S., & Bonnell, I. A. 2012, *MNRAS*, 424, 2599
- Daddi, E., Dannerbauer, H., Liu, D., et al. 2015, *A&A*, 577, A46
- Dame, T. M., Hartmann, D., & Thaddeus, P. 2001, *ApJ*, 547, 792
- Draine, B. T. 2011, *Physics of the Interstellar and Intergalactic Medium*
- Hasegawa, T. I., Mitchell, G. F., Matthews, H. E., & Tacconi, L. 1994, *ApJ*, 426, 215
- Hou, L. G. & Gao, X. Y. 2014, *MNRAS*, 438, 426
- Jayasinghe, T., Dixon, D., Povich, M. S., et al. 2019, *MNRAS*, 1691
- Jiang, B., Chen, Y., Wang, J., et al. 2010, *ApJ*, 712, 1147
- Kaufman, M. J., Wolfire, M. G., Hollenbach, D. J., & Luhman, M. L. 1999, *ApJ*, 527, 795
- Kudo, N., Torii, K., Machida, M., et al. 2011, *PASJ*, 63, 171
- Nishimura, A., Tokuda, K., Kimura, K., et al. 2015, *ApJS*, 216, 18
- Peñaloza, C. H., Clark, P. C., Glover, S. C. O., & Klessen, R. S. 2018, *MNRAS*, 475, 1508
- Polychroni, D., Moore, T. J. T., & Allsopp, J. 2012, *MNRAS*, 422, 2992
- Qin, S.-L., Wang, J.-J., Zhao, G., Miller, M., & Zhao, J.-H. 2008, *A&A*, 484, 361
- Sakamoto, S., Hasegawa, T., Hayashi, M., Handa, T., & Oka, T. 1995, *ApJS*, 100, 125
- Schöier, F. L., van der Tak, F. F. S., van Dishoeck, E. F., & Black, J. H. 2005, *A&A*, 432, 369
- Simpson, R. J., Povich, M. S., Kendrew, S., et al. 2012, *MNRAS*, 424, 2442
- van der Tak, F. F. S., Black, J. H., Schöier, F. L., Jansen, D. J., & van Dishoeck, E. F. 2007, *A&A*, 468, 627
- Watson, C., Povich, M. S., Churchwell, E. B., et al. 2008, *ApJ*, 681, 1341
- Wilson, C. D., Walker, C. E., & Thornley, M. D. 1997, *ApJ*, 483, 210
- Yoda, T., Handa, T., Kohnno, K., et al. 2010, *PASJ*, 62, 1277
- Zhang, C.-P., Li, G.-X., Wyrowski, F., et al. 2016, *A&A*, 585, A117
- Zhang, C.-P., Wang, J.-J., & Xu, J.-L. 2013, *A&A*, 550, A117
- Zhou, P., Chen, Y., Zhang, Z.-Y., et al. 2016, *ApJ*, 826, 34
- Zhou, P., Li, J.-T., Zhang, Z.-Y., et al. 2018, *ApJ*, 865, 6

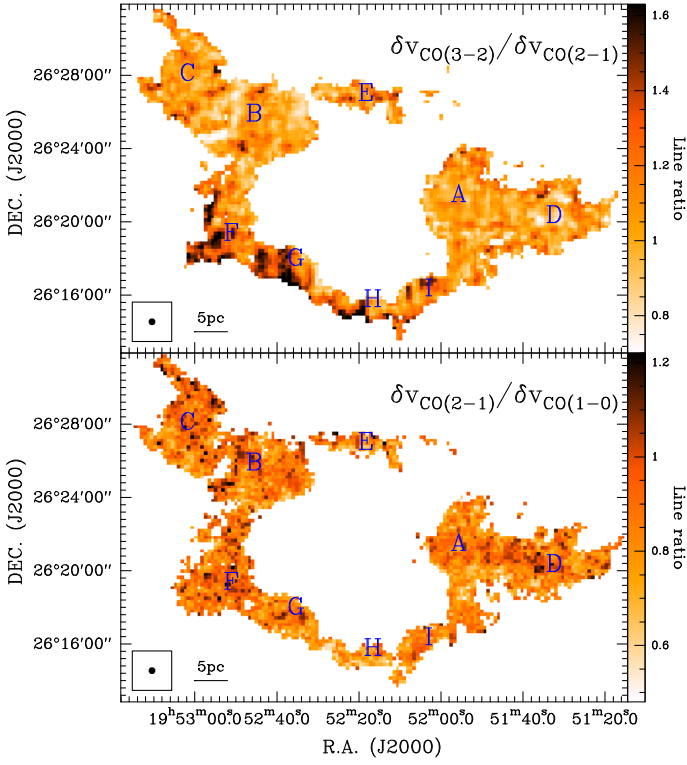


Fig. A.1. Linewidth ratio maps of $\delta v_{\text{CO}(3-2)}/\delta v_{\text{CO}(2-1)}$ (upper) and $\delta v_{\text{CO}(2-1)}/\delta v_{\text{CO}(1-0)}$ (lower). The letters indicate the positions of nine molecular clumps (A, B, ..., and I) in the bubble. The angular resolution is indicated at the bottom-left corner.

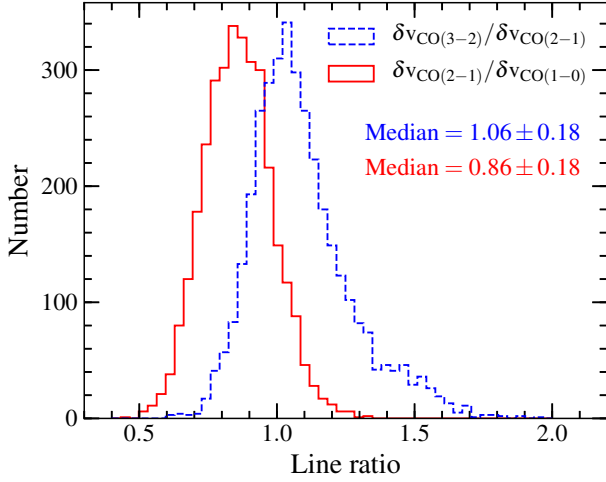


Fig. A.2. Linewidth ratio histograms of $\delta v_{\text{CO}(3-2)}/\delta v_{\text{CO}(2-1)}$ and $\delta v_{\text{CO}(2-1)}/\delta v_{\text{CO}(1-0)}$ for all pixels in Figure A.1.

Appendix A: Linewidth ratio

Figure A.1 displays the linewidth ratio maps of $\delta v_{\text{CO}(3-2)}/\delta v_{\text{CO}(2-1)}$ and $\delta v_{\text{CO}(2-1)}/\delta v_{\text{CO}(1-0)}$. For the clumps F, G, and H in the $\delta v_{\text{CO}(3-2)}/\delta v_{\text{CO}(2-1)}$ map, the outer rims of ringlike shell have a higher linewidth ratio than the inner rims, while it is vice versa for the clump I. For the other clumps, there is no visible line ratio gradient feature. In the $\delta v_{\text{CO}(2-1)}/\delta v_{\text{CO}(1-0)}$ map, it seems that the higher linewidth ratios are located at the clump center positions, and the line ratio gradient is not evident. Figure A.2 displays the linewidth ratio histograms of $\delta v_{\text{CO}(3-2)}/\delta v_{\text{CO}(2-1)}$ and $\delta v_{\text{CO}(2-1)}/\delta v_{\text{CO}(1-0)}$ for

all pixels in Figure A.1. The line ratios of $\delta v_{\text{CO}(3-2)}/\delta v_{\text{CO}(2-1)}$ mostly range from 0.6 to 1.8 with a median of 1.06 ± 0.18 , while $\delta v_{\text{CO}(2-1)}/\delta v_{\text{CO}(1-0)}$ range from 0.5 to 1.3 with a median of 0.86 ± 0.18 . We can also derive the median value of $\delta v_{\text{CO}(3-2)}/\delta v_{\text{CO}(1-0)}$ is around 0.91. Comparison with the linewidth ratios, we will have $\delta v_{\text{CO}(1-0)} > \delta v_{\text{CO}(3-2)} > \delta v_{\text{CO}(2-1)}$ only for their median values. However, generally the linewidth ratios between CO (3 – 2), CO (2 – 1), and CO (1 – 0) are close to unity.